

Phenomenological and Micromechanical Modeling of Anisotropic Effects in Hyperelastic Materials

M. Timmel¹, M. Kaliske², S. Kolling³

¹ DaimlerChrysler AG, EP/SPB, HPC X271, 71059 Sindelfingen
Email: Mario.Timmel@DaimlerChrysler.com

² Technische Universität Dresden
Institut für Statik und Dynamik der Tragwerke, 01062 Dresden
Email: Michael.Kaliske@TU-Dresden.de

³ DaimlerChrysler AG, EP/SPB, HPC X271, 71059 Sindelfingen
Email: Stefan.Kolling@DaimlerChrysler.com

Abstract:

Hyperelastic materials may exhibit anisotropic effects caused by fiber-reinforcement and filler-particles. In the latter case, anisotropy is induced by directional preconditioning during the production process where a microstructural rearrangement takes place. This behaviour is also known as Mullin's effect that can be treated phenomenologically by elastic damage models.

In the framework of the present paper, we discuss a phenomenological approach to model anisotropic behaviour of rubberlike materials. Subsequently, we describe a method to simulate the damage evolution at the microscale where the anisotropy of the material is obtained in a natural way. The damaged material is represented by a soft inclusion embedded in an undamaged matrix material. The growth of the inclusion is formulated in terms of thermodynamic driving forces (also known as material forces) that define the direction of the evolution process.

Keywords:

Hyperelasticity, Anisotropy, Micromechanics, Damage, Material Forces

1 Introduction

Anisotropic effects are important but often neglected effects in the description of the material behaviour of solids. A huge number of materials show anisotropic behaviour such as composites, bio-materials and even single crystals. In rubber-like materials, it is instructive to subdivide anisotropy into three classes:

- 1) material anisotropy,
- 2) geometrically induced anisotropy,
- 3) load induced anisotropy.

In the first class, the material's anisotropy is caused by orientations "inside" the material, e.g. by fibre-reinforcement. In the second class of anisotropy, the orientation is induced purely geometrically and is thus not a material property. This is an engineering approach where the structural geometry is taken into account in a smeared way. Figure 1 shows the treatment of tread pattern as an example.

KALISKE and SCHMIDT [3] describe an anisotropic phenomenological formulation based on the work of SPENCER [11]. In the third class, the material is initially isotropic and orientation is induced during loading, e.g. by reorientation of polymer chains or damage. This phenomenon can be observed, for instance, in particle-filled rubbers with high damping under cyclic loading (also known as Mullins effect). This effect can be described

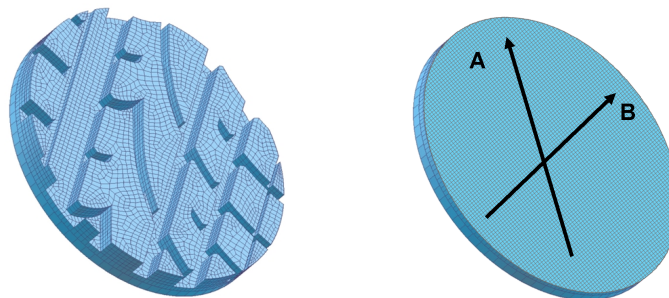


Figure 1: Geometrically anisotropy at tire pattern (left), homogenized part (right) [2]

either phenomenologically by elastic damage models or by a micromechanical formulation. In TIMMEL et al. [13], a two-scale approach has been proposed, where the damaged domain is approximated by an elliptical inclusion. The evolution of inclusion's shape in an isotropic matrix material is described in terms of thermodynamic driving forces acting on the inclusion. In an anisotropic matrix material, the description of the damage accumulation with phenomenological approaches is very difficult. With the help of the two-scale-approach, however, the problem can be solved in a consistent way.

In this paper, we discuss both phenomenological and micromechanical approaches to model anisotropic phenomena in hyperelastic materials. The application of the two-scale damage model is shown, for the first time, for an anisotropic matrix material in the microscale.

2 Phenomenological Approach of Anisotropic Hyperelasticity

2.1 Basic Equations

The constitutive strain energy

$$\Psi = \hat{W}(\underline{\mathbf{C}}, \mathbf{A}, \mathbf{B}) + U(J) \quad (1)$$

depends on the isochoric part of the right CAUCHY-GREEN-Tensor $\underline{\mathbf{C}} = \underline{\mathbf{F}}^T \underline{\mathbf{F}}$, where $\underline{\mathbf{F}} = J^{-1/3} \mathbf{F}$ defines the isochoric deformation gradient with $J = \det \mathbf{F}$ and two constitutive material directions \mathbf{A} and \mathbf{B} , where $\|\mathbf{A}\| = 1$ and $\|\mathbf{B}\| = 1$. According to Equation (1), the strain energy is divided into an isochoric and a volumetric part. For the definition of the compression behaviour, the "penalty" term

$$U(J) = \frac{K}{2} \left(\frac{J^2 - 1}{2} - \ln J \right) \quad (2)$$

is used, where the penalty parameter K corresponds to the bulk modulus that controls the volume change. Based on SPENCER [11], the material directions and the right CAUCHY-GREEN-Tensor can be used to define the irreducible invariants

$$\begin{aligned} \bar{\text{I}} &= \text{tr } \underline{\mathbf{C}}, & \bar{\text{II}} &= 1/2(\text{tr}^2 \underline{\mathbf{C}} - \text{tr } \underline{\mathbf{C}}^2), \\ \bar{\text{IV}} &= \mathbf{A} \cdot \underline{\mathbf{C}} \mathbf{A}, & \bar{\text{V}} &= \mathbf{A} \cdot \underline{\mathbf{C}}^2 \mathbf{A}, \\ \bar{\text{VI}} &= \mathbf{B} \cdot \underline{\mathbf{C}} \mathbf{B}, & \bar{\text{VII}} &= \mathbf{B} \cdot \underline{\mathbf{C}}^2 \mathbf{B}, \\ \bar{\text{VIII}} &= (\mathbf{A} \cdot \mathbf{B}) \mathbf{A} \cdot \underline{\mathbf{C}} \mathbf{B}. \end{aligned} \quad (3)$$

The isotropic part of the material behaviour is described by the first and second invariant in Equation (3). Now, the general isochoric part of the strain energy in Equation (1) can be written in an alternative form

$$\hat{W} = \hat{W}(\bar{\text{I}}, \bar{\text{II}}, \bar{\text{IV}}, \bar{\text{V}}, \bar{\text{VI}}, \bar{\text{VII}}, \bar{\text{VIII}}). \quad (4)$$

A suitable strain energy function is given by

$$\begin{aligned} \hat{W} &= \sum_{i=1}^3 a_i (\bar{\text{I}} - 3)^i + \sum_{j=1}^3 b_j (\bar{\text{II}} - 3)^j + \sum_{k=2}^6 c_k (\bar{\text{IV}} - 1)^k + \sum_{l=2}^6 d_l (\bar{\text{V}} - 1)^l \\ &+ \sum_{m=1}^3 e_m (\bar{\text{VI}} - 3)^m + \sum_{n=2}^6 f_n (\bar{\text{VII}} - 1)^n \end{aligned} \quad (5)$$

which is uncoupled in terms of the invariants. The linear anisotropic part for $k, l = 1$ is not considered to allow for a stress-free reference configuration. The coefficients $a_i, b_j, c_k, d_l, e_m, f_n$ with $i, j, = 1, 2, 3$ and $k, l, m, n = 2, \dots, 6$ present the material parameters. Now, the isochoric stress according to Equation (5) can be calculated by the relation

$$\underline{\mathbf{S}}_{iso} = J^{-\frac{2}{3}} \text{DEV } \tilde{\underline{\mathbf{S}}}, \quad (6)$$

where the operator

$$\text{DEV}(\bullet) = (\bullet) - \frac{1}{3} \left(\underline{\mathbf{C}} : (\bullet) \right) \underline{\mathbf{C}}^{-1} \quad (7)$$

is used and

$$\begin{aligned} \tilde{\underline{\mathbf{S}}} = 2 \frac{\partial W}{\partial \underline{\mathbf{C}}} &= 2 \left(\frac{\partial W}{\partial \bar{\text{I}}} + \bar{\text{I}} \frac{\partial W}{\partial \bar{\text{II}}} \right) \underline{\mathbf{1}} - 2 \frac{\partial W}{\partial \bar{\text{II}}} \underline{\mathbf{C}} + 2 \frac{\partial W}{\partial \bar{\text{IV}}} (\underline{\mathbf{A}} \otimes \underline{\mathbf{A}}) + 2 \frac{\partial W}{\partial \bar{\text{VI}}} (\underline{\mathbf{B}} \otimes \underline{\mathbf{B}}) \\ &+ 2 \frac{\partial W}{\partial \bar{\text{V}}} (\underline{\mathbf{A}} \otimes \underline{\mathbf{C}} \underline{\mathbf{A}} + \underline{\mathbf{C}} \underline{\mathbf{A}} \otimes \underline{\mathbf{A}}) + 2 \frac{\partial W}{\partial \bar{\text{VII}}} (\underline{\mathbf{B}} \otimes \underline{\mathbf{C}} \underline{\mathbf{B}} + \underline{\mathbf{C}} \underline{\mathbf{B}} \otimes \underline{\mathbf{B}}) \\ &+ \frac{\partial W}{\partial \bar{\text{VIII}}} (\underline{\mathbf{A}} \cdot \underline{\mathbf{B}}) (\underline{\mathbf{A}} \otimes \underline{\mathbf{B}} + \underline{\mathbf{B}} \otimes \underline{\mathbf{A}}). \end{aligned} \quad (8)$$

The derivations of the invariants with respect to the right CAUCHY-GREEN-Tensor can be found in SPENCER [11].

The volumetric part of 2nd PIOLA-KIRCHHOFF-stress $\underline{\mathbf{S}}_{vol}$ can be computed by

$$\underline{\mathbf{S}}_{vol} = 2 \frac{\partial U}{\partial J} \frac{\partial J}{\partial \underline{\mathbf{C}}}. \quad (9)$$

2.2 Applications

Anisotropic hyperelastic approaches can be applied for fibre-reinforced rubber materials (see SPENCER [11]) or in the field of biomechanics. Here, the material model presented in Section 2 is used to simplify numerical simulations with geometrical induced anisotropy. At

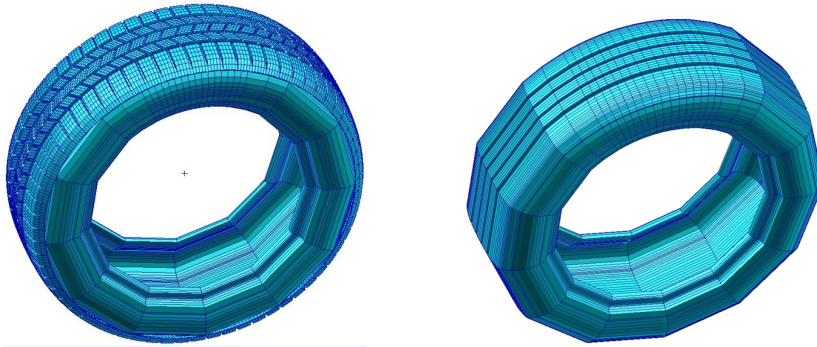


Figure 2: Model with fully discretized tread pattern (left), right: homogenized tire (right)

the left hand side of Figure 2, a fine discretized tire model is depicted. The constitution of the pattern induces anisotropic behaviour. To approach the tire characteristics numerically in a detail, the high resolution results in enormous degrees of freedom. Additionally, a steady-state rolling approach is frequently used in tire simulations (see KALISKE & TIMMEL [4]). In such FEM procedures, a special arbitrary Lagrange-Eulerian (ALE)-formulation is used. However, the ALE-formulation demands an axisymmetric geometry that is lost because of the tread blocks. To improve the efficiency of the FEM-model on the one hand and allow the ALE-formulation on the other hand, the fine pattern is

approached by a homogenous structure. Here, the anisotropic properties have to transfer into the material model: The material directions \mathbf{A} and \mathbf{B} (see Equation (1)) and the corresponding material parameters (see Equation (5)) have to be identified on the basis of experimental data. The material and experimental directions can be compared

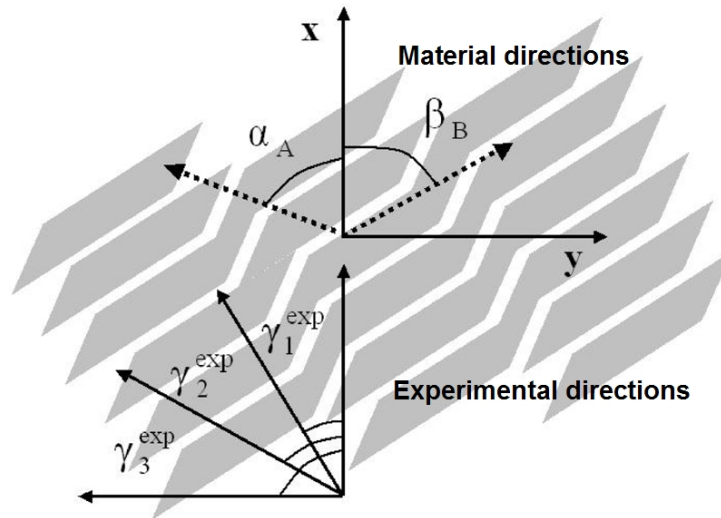


Figure 3: Experimental and material directions of the tread pattern

in Figure 3. In the first step, a chosen tread block with fine resolution will be loaded in different experimental directions. The numerical simulation is performed for several directions $\gamma_i^{\text{exp}} = 0^\circ, 15^\circ, \dots, 180^\circ$. In these directions, a shear-deformation with

$$\underline{\mathbf{F}} = \begin{pmatrix} 1 & \gamma & 0 \\ 0 & 1 & 0 \\ 0 & 0 & 1 \end{pmatrix} \quad (10)$$

and $\max \gamma = 0.7$ is applied to get $P(\gamma_i^{\text{exp}}, \gamma)$ -curves that will be used in the next step in a genetic algorithm to identify the parameters. In the optimization procedure, the material directions \mathbf{A} and \mathbf{B} are calculated with respect to the angle α and β

$$\begin{aligned} \alpha &= \alpha_{\mathbf{A}} + \gamma_i^{\text{exp}} \\ \beta &= \beta_{\mathbf{B}} + \gamma_i^{\text{exp}}. \end{aligned} \quad (11)$$

In Equation (11), $\alpha_{\mathbf{A}}$ and $\beta_{\mathbf{B}}$ define the angle of the material anisotropy which are determined by the algorithm. The corresponding stiffness parameter is identified using this angle. The parameter identification procedure requires a large number of iterations. Therefore, the numerical efficiency can be improved for analytically defined deformations. As can be seen in Figure 4, a good approximation at homogenized elements can be obtained with the identified stiffness parameters and material directions. A detailed description of this application can be found in KALISKE & TIMMEL [4].

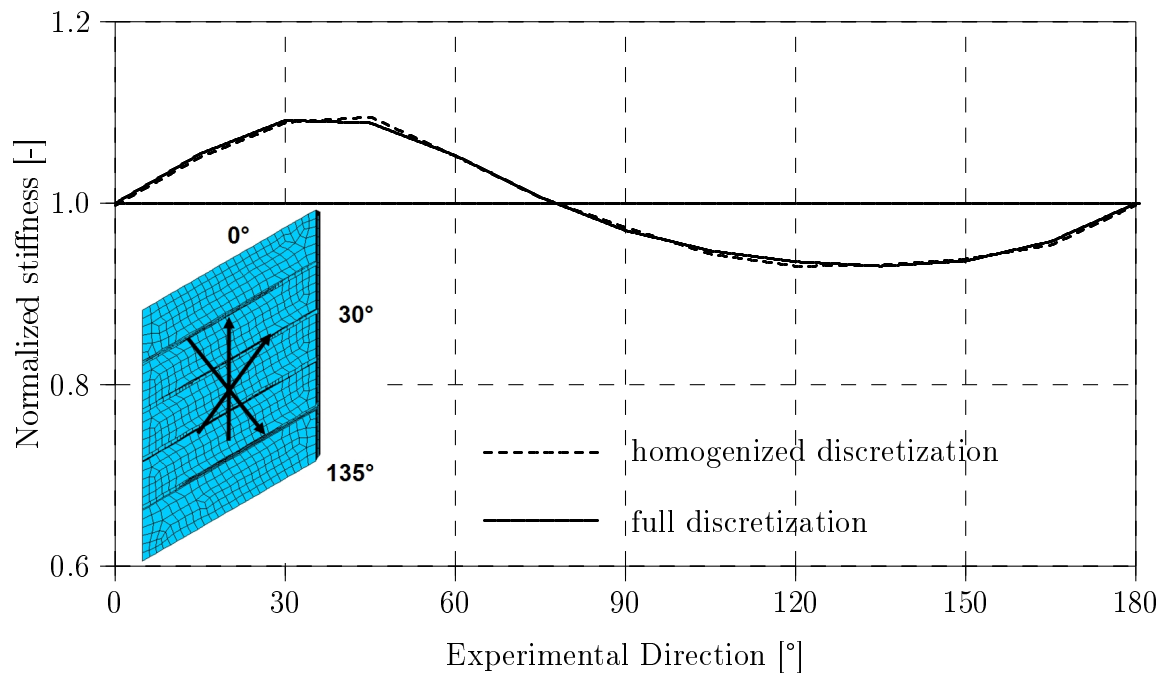


Figure 4: Direction dependent maximum stiffness at full and homogenized discretization

3 Two-Scale Approach

The principle of our two scale damage model is illustrated in Figure 5. Apart from the homogeneous global structure B , we define explicitly a microsystem which consists of a heterogeneous body, whereby B^+ denotes a matrix material with a hyperelastic strain energy density Ψ^+ . A second phase with the volume B^- and the free energy $\Psi^- < \Psi^+$ is considered in the microscale model to represent a material defect. This heterogeneous material results in a macroscopic (homogenized) strain energy $\langle \Psi \rangle$. The microstructure is able to change its configuration during the loading process whereby an expansion of the domain B^- may be expected to minimize the total energy in case of material softening. In the consequence, the homogenized strain energy of the initial configuration B_0 differs from the macrostructure B_t . To model the damage behaviour of the current configuration $\varphi(B_t)$, we develop a method to change the microstructural configuration.

In the following, a model for the description of the evolution of these embedded soft inclusions is presented. The inclusions are geometrically approximated by ellipsoids. This restriction is justified due to frequently appearances of void-like structures and, moreover, numerical investigations can be carried out more efficiently.

3.1 Micromechanical Formulation

For the simulation of the microstructural evolution (i.e. evolution of the inclusion's shape and volume in time), some basic principles are discussed in the following. According to Figure 6, we define a general hyperelastic two phase system in its reference configuration. The phases are separated by a phase boundary S . The vector \mathbf{n} denotes the unit normal

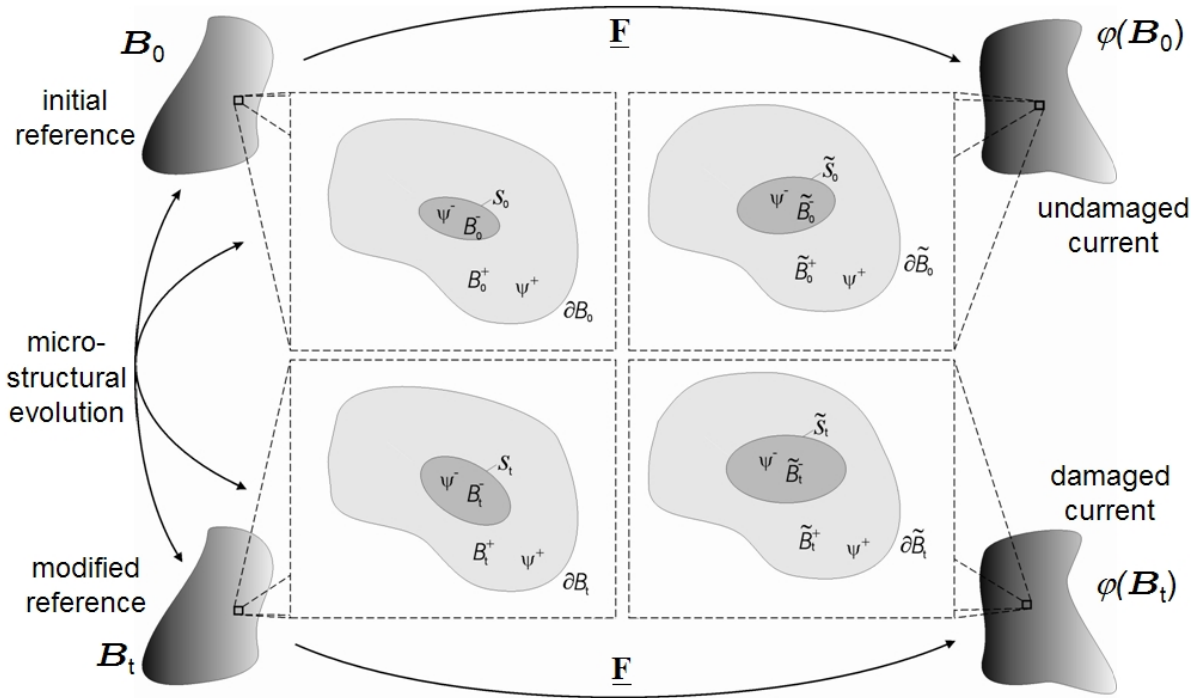


Figure 5: Micro-macroscale-interaction

vector on S and \mathbf{N} is the unit normal on the outer boundary ∂B . The densities of phases are assumed to be identical ($\rho^- = \rho^+ = \rho$), i.e. mass will be conserved and only the stiffnesses differ from each other to define the damaged zone. The loading of the microstructure is either given by a surface traction $\mathbf{T} = \mathbf{P}\mathbf{N}$ (where \mathbf{P} is the first Piola-Kirchhoff stress) or by a prescribed boundary displacement $\mathbf{x} = \mathbf{F}\mathbf{X}$ (where \mathbf{F} is the deformation gradient). Due to the inhomogeneity, the local free energy depends on the material position \mathbf{X} explicitly

$$\Psi(\mathbf{F}, \mathbf{X}) = \begin{cases} \Psi^-(\mathbf{X}) & \forall \mathbf{X} \in B^- \\ \Psi^+(\mathbf{X}) & \forall \mathbf{X} \in B^+ \end{cases} \quad (12)$$

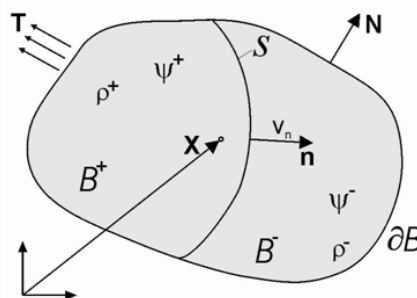


Figure 6: Two-phase-model

The dissipation inequality describes the movement of the phase boundary S expressed in terms of the velocity v_n in normal direction. The corresponding thermomechanical formulations of a moving phase boundary S will be represented in the following. For a detailed derivation, the reader is referred to [10] and the literature cited therein. The momentum balance is given by

$$\begin{aligned} \text{Div} \underline{\mathbf{P}} + \rho \ddot{\mathbf{x}} &= \mathbf{0} && \text{in } B^-/B^+ \\ \llbracket \underline{\mathbf{P}} \mathbf{n} \rrbracket + \rho \llbracket \dot{\mathbf{x}} \rrbracket v_n &= \mathbf{0} && \text{on } S \end{aligned} \quad (13)$$

where body forces \mathbf{f} are neglected and $\llbracket \cdot \rrbracket = (\cdot)^+ - (\cdot)^-$ denotes the jump of a quantity across the phase boundary. The rotational momentum balance yields the symmetry

$$\underline{\mathbf{P}} \underline{\mathbf{F}}^T = \underline{\mathbf{F}} \underline{\mathbf{P}}^T \quad (14)$$

where no additional condition on the phase boundary is pointed out. The energy balance can be given by

$$\begin{aligned} \rho \dot{u} - \underline{\mathbf{P}} : \dot{\underline{\mathbf{F}}} &= 0 && \text{in } B^-/B^+ \\ \rho \llbracket u + \frac{1}{2} |\dot{\mathbf{x}}|^2 \rrbracket v_n + \llbracket (\underline{\mathbf{P}} \mathbf{n}) \cdot \dot{\mathbf{x}} \rrbracket &= 0 && \text{on } S \end{aligned}, \quad (15)$$

where u denotes the specific internal energy. Finally, the entropy balance of the two phase system is stated by

$$\begin{aligned} \rho \dot{\eta} \Theta - \omega_B \Theta &= 0 && \text{in } B^-/B^+ \\ \rho \Theta \llbracket \dot{\eta} \rrbracket v_n - \omega_S \Theta &= 0 && \text{on } S \end{aligned}. \quad (16)$$

Here, η is the entropy density and Θ denotes the absolute temperature. ω_B and ω_S describe the production of entropy in volume and on the phase boundary, respectively. Due to the restriction of identic densities ($\rho^+ = \rho^-$), the mass balance is presumed. In accordance with the second law of thermodynamics ($\omega_B \geq 0$, $\omega_S \geq 0$) and defining the free energy $\Psi = \rho(u - \eta\Theta)$, Equations (15)₁ and (16)₁ result in the dissipation inequality in the bulk

$$\underline{\mathbf{P}} : \dot{\underline{\mathbf{F}}} - \dot{\Psi} = \omega_B \Theta \geq 0. \quad (17)$$

With Equations (15)₂ and (16)₂, we obtain the dissipation inequality on the phase interface

$$\llbracket \Psi + \frac{1}{2} \rho |\dot{\mathbf{x}}|^2 \rrbracket v_n + \llbracket (\underline{\mathbf{P}} \mathbf{n}) \cdot \dot{\mathbf{x}} \rrbracket = \omega_S \Theta \geq 0. \quad (18)$$

The first part of Equation (18) corresponds to the total energy as the sum of free energy and kinetic energy. Henceforth, the middle term of (18) shall be reformulated (see [8]). In this context, we use the compatibility $\llbracket \dot{\mathbf{x}} \rrbracket = -v_n \llbracket \underline{\mathbf{F}} \rrbracket \mathbf{n}$, the momentum balance (Equation (13)), and the identity $\llbracket ab \rrbracket = \llbracket a \rrbracket \langle\langle b \rangle\rangle + \langle\langle a \rangle\rangle \llbracket b \rrbracket$, where $\langle\langle \cdot \rangle\rangle = \frac{1}{2}[(\cdot)^+ + (\cdot)^-]$. At first, the middle term is modified by

$$\begin{aligned} \llbracket (\underline{\mathbf{P}} \mathbf{n}) \cdot \dot{\mathbf{x}} \rrbracket &= -\rho v_n \llbracket \dot{\mathbf{x}} \rrbracket \langle\langle \dot{\mathbf{x}} \rangle\rangle - v_n \llbracket \underline{\mathbf{F}} \rrbracket \langle\langle \underline{\mathbf{P}} \mathbf{n} \rangle\rangle \\ &\quad - v_n \langle\langle \underline{\mathbf{F}} \mathbf{n} \rangle\rangle \cdot \underbrace{\llbracket \underline{\mathbf{P}} \rrbracket + \rho \llbracket \dot{\mathbf{x}} \rrbracket v_n}_{=0}, \end{aligned} \quad (19a)$$

where the last part of Equation (19a) vanishes due to (13)₂. With

$$\begin{aligned} -\rho v_n^2 \langle \underline{\mathbf{F}} \mathbf{n} \rangle [\dot{\mathbf{x}}] &= -\rho v_n [\dot{\mathbf{x}}] \langle \dot{\mathbf{x}} \rangle \\ &\quad - \rho v_n^2 [\underline{\mathbf{F}} \mathbf{n}] \langle \dot{\mathbf{x}} \rangle - \rho v_n^2 [\underline{\mathbf{F}} \mathbf{n}] \langle \dot{\mathbf{x}} \rangle \end{aligned}$$

the reformulation of (19a) finally yields

$$\begin{aligned} [(\underline{\mathbf{P}} \mathbf{n}) \cdot \dot{\mathbf{x}}] &= -2\rho v_n [\dot{\mathbf{x}}] \langle \dot{\mathbf{x}} \rangle \\ &\quad - v_n [\underline{\mathbf{F}} \mathbf{n}] \langle \underline{\mathbf{P}} \mathbf{n} \rangle - v_n \langle \underline{\mathbf{F}} \mathbf{n} \rangle [\underline{\mathbf{P}} \mathbf{n}] \\ &\quad - \rho v_n^2 [\underline{\mathbf{F}} \mathbf{n}] \langle \dot{\mathbf{x}} \rangle - \rho v_n^2 \langle \underline{\mathbf{F}} \mathbf{n} \rangle [\dot{\mathbf{x}}] \\ &= -\rho v_n [|\dot{\mathbf{x}}|^2] \\ &\quad - v_n [\underline{\mathbf{F}}^T \underline{\mathbf{P}}] \mathbf{n} \\ &\quad - \rho v_n^2 [\underline{\mathbf{F}}^T \dot{\mathbf{x}}] \cdot \mathbf{n} . \end{aligned} \tag{19b}$$

Thus, the dissipation inequality on the phase boundary (18) can be written in the modified form

$$\underbrace{(\mathbf{n} \cdot [\underline{\mathbf{M}}] \mathbf{n} - v_n \rho \mathbf{n} \cdot [\underline{\mathbf{F}}^T \dot{\mathbf{x}}])}_{\tau_n} v_n = \omega_S \Theta \geq 0. \tag{20}$$

In Equation (20), the quantity

$$\underline{\mathbf{M}} = \left(\Psi - \frac{1}{2} \rho |\dot{\mathbf{x}}|^2 \right) \underline{\mathbf{1}} - \underline{\mathbf{F}}^T \underline{\mathbf{P}} \tag{21}$$

is referred to as dynamic energy momentum tensor [1]. τ_n defines the driving force on S . In the next step, we consider the Lagrangian \mathcal{L} of the two phase system

$$\mathcal{L} = T - \Psi = \frac{1}{2} \rho |\dot{\mathbf{x}}|^2 - \Psi(\underline{\mathbf{F}}, \mathbf{X}) \tag{22}$$

that is defined as the difference of the kinetic energy and the free energy. The change of the Lagrangian with respect to a translation of a material point can be investigated by computing the gradient

$$\begin{aligned} \nabla_{\mathbf{X}} \mathcal{L} &= \nabla_{\mathbf{X}} T - \nabla_{\mathbf{X}} \Psi \\ &= \rho (\nabla_{\mathbf{X}} \mathbf{v})^T \mathbf{v} - \underline{\mathbf{P}} : \nabla_{\mathbf{X}} \underline{\mathbf{F}} - \frac{\partial \Psi}{\partial \mathbf{X}} \Big|_{\text{expl.}} . \end{aligned} \tag{23}$$

In Equation (23), the explicit derivative of the energy Ψ with respect to \mathbf{X} yields the driving force. If we use the compatibility $\nabla_{\mathbf{X}} \dot{\mathbf{x}} = \dot{\underline{\mathbf{F}}}$, the local balance of momentum in volume according to Equation (13)₂, the identity $\underline{\mathbf{P}} : \nabla_{\mathbf{X}} \underline{\mathbf{F}} = \text{Div}(\underline{\mathbf{F}}^T \underline{\mathbf{P}}) - \underline{\mathbf{F}}^T \text{Div} \underline{\mathbf{P}}$ and $\nabla_{\mathbf{X}} \mathcal{L} = \text{Div}(\mathcal{L} \underline{\mathbf{1}})$, we achieve the configurational force balance in the volume

$$\underbrace{(-\rho \overline{\underline{\mathbf{F}}^T \dot{\mathbf{x}}})}_{:= -\dot{\underline{\mathbf{p}}}} = \text{Div} \underbrace{(-\mathcal{L} \underline{\mathbf{1}} - \underline{\mathbf{F}}^T \underline{\mathbf{P}})}_{\underline{\mathbf{M}}} + \underbrace{\frac{\partial \Psi}{\partial \mathbf{X}} \Big|_{\text{expl.}}}_{\underline{\mathbf{g}}_B} \tag{24}$$

(see [7]), where we introduce the configurational force \mathbf{g}_B and the pseudo momentum vector \mathbf{p} . To show that (24) is the global form of (20), we consider the generalized transport theorem

$$\frac{d}{dt} \int_B \rho \Phi \, dV = \int_{\partial B} \Omega \cdot \mathbf{N} \, dA + \int_A \Pi_S \, dA + \int_B \Pi_V \, dV, \quad (25)$$

where $A \subset S$ and its local form can be given by

$$\begin{aligned} \rho \dot{\Phi} &= \text{Div} \Omega + \Pi_V && \text{in } B^-/B^+ \\ -\rho \llbracket \Phi \rrbracket_{\mathbf{v}_n} &= \llbracket \Omega \rrbracket_{\mathbf{n}} + \Pi_S && \text{on } S \end{aligned}, \quad (26)$$

(see [10]). It can be seen from Equations (24) and (26)₁ that the general quantity Φ can be associated with $(-\underline{\mathbf{F}}^T \dot{\mathbf{x}})$. In the same way, Ω corresponds to the energy momentum tensor $\underline{\mathbf{M}}$ and Π_B corresponds to the configurational force in volume \mathbf{g}_B .

In the consequence, Equation (26)₂ yields the configurational momentum balance on the phase boundary

$$\rho \llbracket \underline{\mathbf{F}}^T \dot{\mathbf{x}} \rrbracket_{\mathbf{v}_n} = \llbracket \underline{\mathbf{M}} \rrbracket_{\mathbf{n}} + \mathbf{g}_S \quad \text{on } S. \quad (27)$$

Assuming that the interface dissipation vanishes in Equation (20) (i.e. $\omega_S = 0$), Equation (20) represents the normal component of the vector in (27). Thus we have established the identity

$$\tau_n = -\mathbf{n} \cdot \mathbf{g}_S = \mathbf{n} \cdot \llbracket \underline{\mathbf{M}} \rrbracket_{\mathbf{n}} - \rho \mathbf{n} \cdot \llbracket \underline{\mathbf{F}}^T \dot{\mathbf{x}} \rrbracket_{\mathbf{v}_n}. \quad (28)$$

3.2 Evolution Equations

For the temporal evolution of the microstructure (i.e. growth of the damaged zone in dependence of the applied load), an evolution equation is formulated in terms of configurational forces. For this purpose, the local dissipation inequality (20) is integrated over the entire phase boundary

$$\mathcal{D} = \int_S \tau_n \mathbf{v}_n \, dA \geq 0. \quad (29)$$

After parametrization of the ellipsoidal shape of the inclusion (see Figure 7) by the vector $\boldsymbol{\chi} = \hat{\boldsymbol{\chi}}(\rho_1, \rho_2, V, \varphi)$, Equation (29) can be rewritten as

$$\begin{aligned} \mathbf{v}_n &= \hat{\boldsymbol{\chi}}(\rho_1, \rho_2, V, \varphi) \cdot \mathbf{n} \\ &= \left(\frac{\partial \boldsymbol{\chi}}{\partial \rho_1} \cdot \mathbf{n} \right) \dot{\rho}_1 + \left(\frac{\partial \boldsymbol{\chi}}{\partial \rho_2} \cdot \mathbf{n} \right) \dot{\rho}_2 + \left(\frac{\partial \boldsymbol{\chi}}{\partial V} \cdot \mathbf{n} \right) \dot{V} + \left(\frac{\partial \boldsymbol{\chi}}{\partial \varphi} \cdot \mathbf{n} \right) \dot{\varphi} \end{aligned} \quad (30)$$

where φ represents the angle between in $X_1 - X_3$ -plane (see [8] and [5] for details). The quantities V , $\rho_1 = a/b$ and $\rho_2 = b/c$ denote volume and aspect ratios of the inclusion with the semi-axes of the ellipsoid a , b and c . With Equations (29) and (30), the global dissipation inequality yields

$$\begin{aligned} \mathcal{D} &= \int_S \tau_n \left[\left(\frac{\partial \boldsymbol{\chi}}{\partial \rho_1} \cdot \mathbf{n} \right) \dot{\rho}_1 + \left(\frac{\partial \boldsymbol{\chi}}{\partial \rho_2} \cdot \mathbf{n} \right) \dot{\rho}_2 + \left(\frac{\partial \boldsymbol{\chi}}{\partial V} \cdot \mathbf{n} \right) \dot{V} + \left(\frac{\partial \boldsymbol{\chi}}{\partial \varphi} \cdot \mathbf{n} \right) \dot{\varphi} \right] dA \\ &= \tau_{\rho_1} \dot{\rho}_1 + \tau_{\rho_2} \dot{\rho}_2 + \tau_V \dot{V} + \tau_\varphi \dot{\varphi} \geq 0. \end{aligned} \quad (31)$$

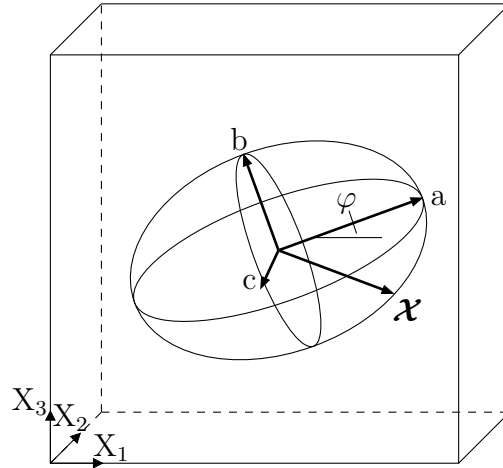


Figure 7: Parametrization of the inclusions

In Equation (31), the quantities τ_V , τ_{ρ_1} , τ_{ρ_2} and τ_φ represent the consistent driving force with respect to the modification of volume and shape and rotation.

To change the inclusion's configuration, appropriate relations $\dot{\rho}_1 = f(\tau_{\rho_1})$, $\dot{\rho}_2 = f(\tau_{\rho_2})$, $\dot{V} = f(\tau_V)$ and $\dot{\varphi} = f(\tau_\varphi)$ that fulfil the dissipation inequality (31) have to be chosen. In this context, the physical behaviour of voids has to be taken into account, e.g. void growth is suppressed for hydrostatic pressure. Though, an evolution in shape is admissible. This means that the inclusion is able to change its shape in vertical direction during horizontal loading and vice versa. Furthermore, the rate of shape modification depends additionally on the current volume in the case of volume evolution. To avoid this effect, we relate τ_{ρ_1} and τ_{ρ_2} to the current inclusion's volume by

$$\dot{\rho}_1 = \alpha_{\rho_1} \tau_{\rho_1} \frac{V_0}{V} \quad \Leftrightarrow \quad \dot{\rho}_2 = \alpha_{\rho_2} \tau_{\rho_2} \frac{V_0}{V} \quad (32)$$

with the material parameters $\alpha_{\rho_1}, \alpha_{\rho_2} > 0$. In Equation (32), V_0 denotes the initial volume of the inclusion. Other relations that fulfil the dissipation inequality (31) are, of course, also possible. In the same way as given in Equation (32), we introduce a relation to evolve the angle φ

$$\dot{\varphi} = \alpha_\varphi \tau_\varphi \frac{V_0}{V}. \quad (33)$$

Based on Equations (32) and (33) and due to (31), we also have to fulfil the constraint

$$\tau_V \dot{V} \geq 0 \quad \text{if } \tau_V \geq 0. \quad (34)$$

In consequence, we allow void growth in the case of a new exceeding amount of τ_V only. This approach coincides with the basic idea of damage evolution in phenomenological models (see TIMMEL et al. [13]). As a suitable relation we use

$$V = V(\beta) = V_0 + (V_{\max} - V_0)(1 - \exp(-\beta/\eta)). \quad (35)$$

The quantity η denotes a saturation parameter to control the rate of void growth. The remaining quantity

$$\beta = \beta(t) = \max_{s \in [0, t]} \tau_V(s) \quad (36)$$

denotes the maximum driving force attained up to the current time t . Consequently, the inequality (31) is preserved.

According to Equation (36), τ_V depends on the boundary position. Since "self growth" of the inclusion may occur under constant loads, we modify the evolution law by relating τ_V to the current surface

$$\beta(t) = \max_{s \in [0, t]} \left[\tau_V(s) \frac{A(0)}{A(s)} \right] \quad (37)$$

where $A(s) = \int_{S(s)} dA$. Moreover, void growth at hydrostatic compression has also to be avoided, though configurational forces cannot distinguish between compression pressure or dilatation. Therefore, we use the applied strain $\underline{\mathbf{E}}^\infty = 0.5 \left((\underline{\mathbf{F}}^\infty)^T \underline{\mathbf{F}}^\infty - \underline{\mathbf{1}} \right)$ as an additional constraint. With the aid of McCauley's brackets defined by

$$\langle \text{tr} \underline{\mathbf{E}}^\infty \rangle = 0.5(\text{tr} \underline{\mathbf{E}}^\infty) + 0.5 |(\text{tr} \underline{\mathbf{E}}^\infty)|, \quad (38)$$

we extend the evolution Equation (37) to give

$$\beta(t) = \max_{s \in [0, t]} \left[\tau_V(s) \frac{A(0)}{A(s)} \frac{\langle \text{tr} \underline{\mathbf{E}}^\infty \rangle}{\text{tr} \underline{\mathbf{E}}^\infty} \right]. \quad (39)$$

3.3 Critical Volume

If the damaged zone exceeds a critical value V_{crit} , the material is not able to withstand further loading and thus fracture occurs. This critical value is comparable to the upper bound of the damage variable d in phenomenological models. To avoid further void growth beyond the threshold value V_{crit} , we define an additional penalty term

$$\Pi_{\text{pen}} = (0.5p(V - V_{\text{crit}}) + 0.5p(|V - V_{\text{crit}}|))^m \quad (40)$$

where any values larger than V_{crit} are penalized by a factor p so that the current volume does not exceed the critical volume. Derivation of Equation (40) with respect to the volume leads to a modification of the driving forces

$$\mathcal{D} = \left(\tau_V - \frac{\partial \Pi_{\text{pen}}}{\partial V} \right) \dot{V} \geq 0. \quad (41)$$

3.4 Homogenization

An important issue of two scale simulations is the transfer of field quantities between the scales. The macrostresses and macrostrains of the upper scale are related to the stresses and strains of the microscale. An important quantity which yields the information of the

loading state is the deformation gradient $\underline{\mathbf{F}}$. Due to microstructural inhomogeneities, its microscopic average

$$\underline{\mathbf{F}}_{\text{mac}} = \langle \underline{\mathbf{F}}_{\text{mic}} \rangle = \langle \underline{\mathbf{F}} \rangle = \frac{1}{V} \int_B \underline{\mathbf{F}}(\mathbf{X}) \, dV \quad (42a)$$

corresponds to the macroscopic value. Based on Gauss' theorem, we modify Equation (42a) and obtain

$$\langle \underline{\mathbf{F}} \rangle = \frac{1}{V} \int_{\partial B} \mathbf{x} \otimes \mathbf{N} \, dA = \underline{\mathbf{1}} + \frac{1}{V} \int_{\partial B} \mathbf{u} \otimes \mathbf{N} \, dA. \quad (42b)$$

With a constant displacement gradient $\underline{\mathbf{H}} = \text{const.}$ and $\mathbf{u}|_{\partial B} = \underline{\mathbf{H}} \cdot \mathbf{X}$, relation (42b)₂ can be reformulated to

$$\langle \underline{\mathbf{F}} \rangle = \underline{\mathbf{1}} + \frac{1}{V} \int_{\partial B} (\underline{\mathbf{H}} \cdot \mathbf{X}) \otimes \mathbf{N} \, dA = \underline{\mathbf{1}} + \underline{\mathbf{H}} = \underline{\mathcal{F}} \quad (42c)$$

(see [6]).

To homogenize the stress in a similar way, we are restricted to a stress quantity which is defined in the reference configuration. Like defined in Equation (42a), the transposed of the first Piola Kirchhoff stress of the macroscale

$$\underline{\mathbf{P}}_{\text{mac}}^{\text{T}} = \langle \underline{\mathbf{P}}_{\text{mac}}^{\text{T}} \rangle = \langle \underline{\mathbf{P}}^{\text{T}} \rangle = \frac{1}{V} \int_B \underline{\mathbf{P}}^{\text{T}}(\mathbf{X}) \, dV \quad (43a)$$

can be computed by averaging of the microscale values. Based on the momentum balance (Equation (13), body forces are neglected), we can use the identity $\text{Div}(\mathbf{X} \otimes \underline{\mathbf{P}}) = \underline{\mathbf{P}}^{\text{T}} - \mathbf{X} \otimes \rho \ddot{\mathbf{x}}$ as well as Gauss' theorem again, to modify Equation (43a) to

$$\langle \underline{\mathbf{P}}^{\text{T}} \rangle = \frac{1}{V} \int_{\partial B} \mathbf{X} \otimes \underline{\mathcal{P}} \cdot \mathbf{N} \, dA + \frac{1}{V} \int_B \mathbf{X} \otimes \rho \ddot{\mathbf{x}} \, dV, \quad (43b)$$

where $\underline{\mathcal{P}} = \text{const.}$ is defined as the First Piola Kirchhoff stress on the boundary in case of a boundary traction $\mathbf{T}|_{\partial B} = \underline{\mathcal{P}} \cdot \mathbf{N}$. With $\text{Div}(\mathbf{X} \otimes \underline{\mathcal{P}}) = \underline{\mathcal{P}}^{\text{T}} - \mathbf{X} \otimes \rho \ddot{\mathbf{x}}$, we finally obtain the correlation

$$\langle \underline{\mathbf{P}}^{\text{T}} \rangle = \underline{\mathcal{P}}^{\text{T}} + \frac{1}{V} \int_B \mathbf{X} \otimes \rho \ddot{\mathbf{x}} \, dV. \quad (43c)$$

Since the Cauchy stress is required, we use the mean value of first Piola Kirchhoff stress according to Equation (43c) and the relation

$$\langle \underline{\boldsymbol{\sigma}} \rangle = (\det \langle \underline{\mathbf{F}} \rangle)^{-1} \langle \underline{\mathbf{F}} \rangle \langle \underline{\mathbf{P}}^{\text{T}} \rangle \quad (44)$$

(see [9]). Once the boundary value problem is solved on the microscale, the mean Cauchy stress can thus be transferred to the macroscale.

3.5 Numerical Implementation into FEM

In the considered hyperelastic materials, analytical solutions for the inclusion problem are, in general, not known. We therefore use a finite element procedure to calculate the driving force on the inclusion using the weak formulation of the configurational momentum balance according to Equation (24). Due to finite element discretization of the structure, the balance equation in volume B has to be used.

After multiplying with a test function $\boldsymbol{\eta}$ and integration over the volume, we obtain

$$\int_B \left(\rho(\overline{\mathbf{F}^T \dot{\mathbf{x}}}) + \text{Div } \underline{\mathbf{M}} + \mathbf{g} \right) \cdot \boldsymbol{\eta} dV = 0. \quad (45)$$

With $(\text{Div } \underline{\mathbf{M}}) \cdot \boldsymbol{\eta} = \text{Div}(\underline{\mathbf{M}} \cdot \boldsymbol{\eta}) - \underline{\mathbf{M}} : \nabla_{\mathbf{x}} \boldsymbol{\eta}$ and Gauss' theorem $\int_B \text{Div}(\underline{\mathbf{M}} \cdot \boldsymbol{\eta}) dV = \int_{\partial B} \underline{\mathbf{M}} \mathbf{n} \cdot \boldsymbol{\eta} dA$, Equation (45) can be rearranged to give

$$\int_B \left[\rho(\overline{\mathbf{F}^T \dot{\mathbf{x}}}) \cdot \boldsymbol{\eta} - \underline{\mathbf{M}} : \nabla_{\mathbf{x}} \boldsymbol{\eta} + \mathbf{g} \cdot \boldsymbol{\eta} \right] dV = 0 \quad (46)$$

where we took into account that the test function $\boldsymbol{\eta}$ vanishes on the boundary ∂B . Henceforth, with an approximation of the test function in each finite element Ω by nodal values $\boldsymbol{\eta}^l$ and shape functions N^l we get the discrete configurational force

$$\mathbf{G}^l = \bigcup_{e=1}^{n_e} \int_{\Omega} \left\{ \underline{\mathbf{M}} \nabla_{\mathbf{x}} N^l - \rho(\overline{\mathbf{F}^T \dot{\mathbf{x}}}) N^l \right\} d\Omega \quad (47)$$

where the operator \bigcup denotes the assembling of all adjacent elements of the node l . The discrete driving force on a phase boundary can be computed according to Equation (28)₁ by multiplying with the normal vector on the phase boundary

$$\mathcal{T}_n^l = -\mathbf{n} \cdot \mathbf{G}^l. \quad (48)$$

A rather complex task is the transfer of the information between the micro- and the macroscale. At first, LS-DYNA gives the deformation of the macroscale. In the user-interface, the program stops until the microscale is analyzed. The macrostructural deformation will be used to move the boundaries of the microstructure. In Figure 8, a deformed and undeformed configuration of a microstructure is shown. In the last deformation-step, the configurational forces will be computed (Figure 9 shows the distribution of configurational forces for the deformed configuration in Figure 8).

With the help of evolution equations of Section 3.2, we modify the geometrical parameters of the inclusion. In the consequence, the complete discrete configuration of inclusion has to be changed. Due to the modification of all inner nodes in the microscale, this results in a new meshing procedure for the general case (see MUELLER [8]).

However, the restriction on ellipsoidal inclusions allows an analytical mesh-modification where the inner nodes are modified by a linear extra- and interpolation. In the following we like to discuss the procedure based on a 2D example as shown in Figure 10: The left

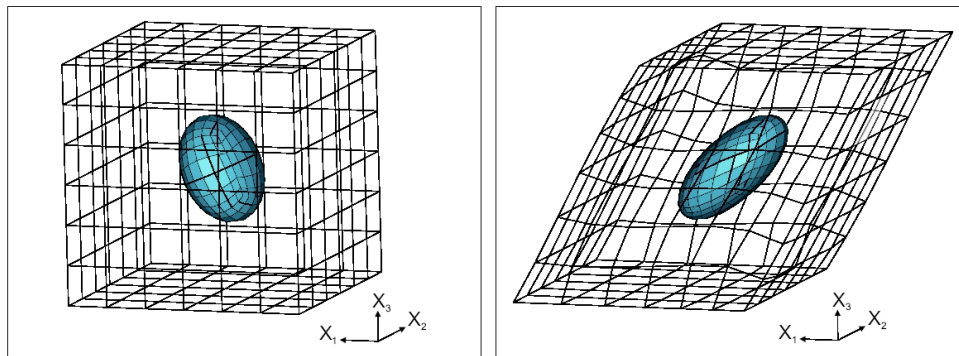
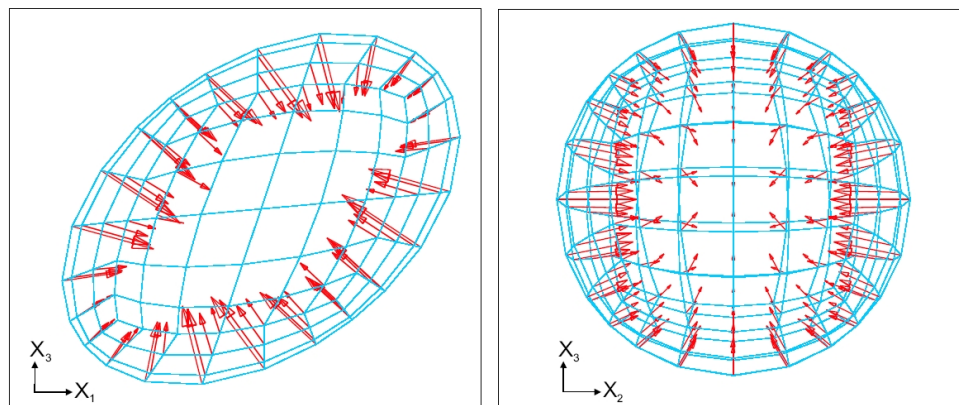


Figure 8: Representative Microstructure, undeformed (left), deformed (right)

Figure 9: Distribution of materials forces \mathbf{G}

hand side shows the discrete undeformed reference configuration where the boundary of the inclusion can be described mathematically. On the right hand side, the boundary of a modified inclusion is depicted.

To change the coordinates of point 3, we have to calculate the angle Φ which supports the computation of the intersection points 2 (on the modified inclusion boundary) and intersection point 1 (on the current inclusion's boundary). The comparison of the intersection points yields a horizontal and vertical difference Δh and Δv . In the second step, a triangular weighting function is defined starting in point 1 (value=1) and ending in point 4 (value=0). The dislocation of point 3 can then be calculated by multiplication with the value of the weighting function in point 3. This procedure has to be carried out for all points concerning the matrix material. Within the inclusion, the triangular weighting function gets the maximum in point 1 and zero in point 0.

In the consequence of this procedure, the finite elements of the inclusion expand and those of matrix shrink. At the lower part of Figure 10, the modified mesh of the microscale is depicted. While the modification of the microstructure is required for the next calculation

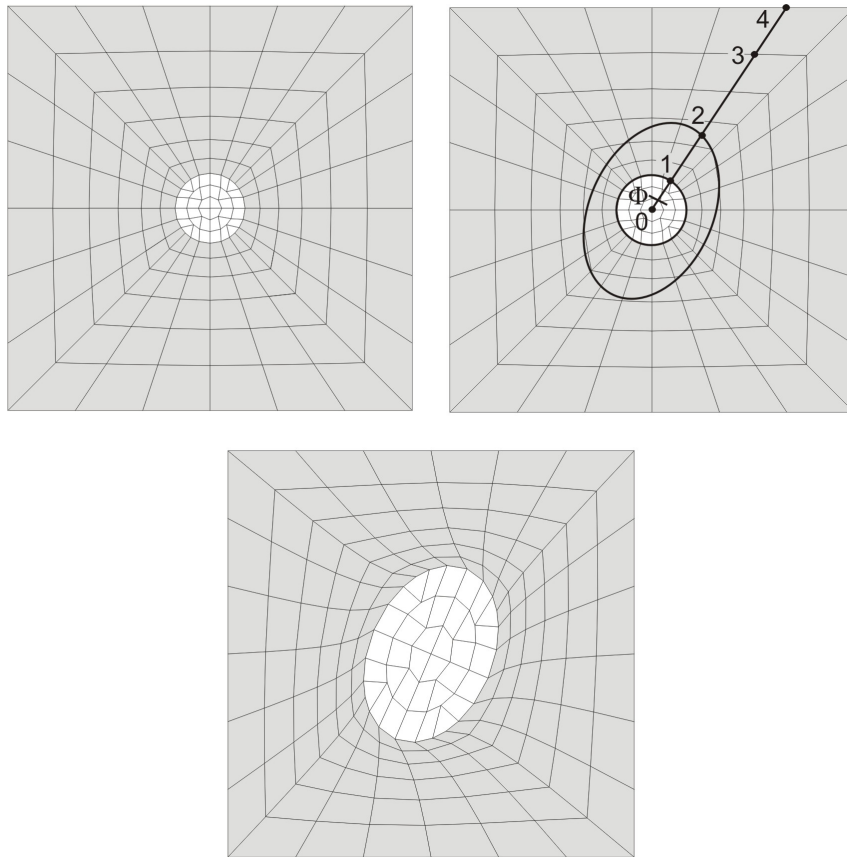


Figure 10: Mesh-modification of the microstructure

step, the stress of all elements has to be averaged by

$$\langle \underline{\mathbf{P}}_n \rangle = \frac{\sum_{e=1}^{n_e} \underline{\mathbf{P}}_n \det J_n}{\sum_{e=1}^{n_e} \det J_n} \quad (49)$$

at the end of the current microstructure analysis. With the help of Equation (44), the averaged first Piola-Kirchhoff stress of the microscale can be converted to the averaged CAUCHY-stress by

$$\langle \underline{\boldsymbol{\sigma}}_n \rangle = (\det \langle \underline{\mathbf{F}}_n \rangle)^{-1} \langle \underline{\mathbf{F}}_n \rangle \langle \underline{\mathbf{P}}_n^T \rangle, \quad (50)$$

to transfer the material response to the macroscale (Equation (50)). Now, the calculation of microscale can be stopped and the analysis of the microstructure for the next time-step under consideration follows. In Figure 11, the algorithm is depicted in a compact form.

3.6 Application

In this section, we discuss some examples with microstructural evolution at hyperelastic material. In particular, it is shown that a material with isotropic behavior at the microscale exhibits anisotropic overall properties due to microstructural evolution.

```

{ loop (time)  $t_0 \leq t_n \leq t_{\text{end}}$ 
  { loop (elements)  $e = 1, n_e$ 
    1. calculation of boundary – deformation of microstructure
       $\mathbf{u}_{\text{mic}}^n|_{\partial B_0} = (\mathbf{F}_e^n - \mathbf{1}) \mathbf{X}_{\text{mic}}^n|_{\partial B_0}$  with  $\mathbf{X}_{\text{mic}}^n|_{\partial B_0} = \text{const.}$ 
    2. Assembling of microstruktue – inputdeck
      • modification of microstructure – nodals by  $\mathbf{X}_{\text{mic}}^n$ 
      • modification of loadcurves by  $\mathbf{u}_{\text{mic}}^n|_{\partial B_0}$ 
      • Modification of end – time – step  $t_n$ 
    3. FE – microstructure – analysis
      • calculation of element – stress  $\mathbf{P}_n$ 
      • Averaging of element – stress according to Equation (49)
      • calculation of configurational forces according to Chapter 3.1
      • mikrostruktural evolution  $\mathbf{X}_{\text{mic}}^{n+1}$  according to Chapter 3.2
    4. return of element – stress
       $\underline{\sigma}_n = \langle \underline{\sigma}_n \rangle$ 
  }
}

```

Figure 11: Twoscale-FEM-algorithm

3.6.1 Isotropic Matrix Material

As a first example, we present a 2-dimensional microstructure discretized with 477 finite elements. The material is modelled by YEOH's approach [14] using the parameters $C_1^+ = 1.0 \text{ N/mm}^3$, $C_2^+ = 2.0 \text{ N/mm}^3$ and $C_3^+ = 0.0 \text{ N/mm}^3$ for the matrix phase. The soft inclusion is modelled by the relations $C_1^- = (1/100)C_1^+$ and $C_2^- = (1/100)C_2^+$. The system is loaded by a prescribed boundary deformation using a triangular strain-time-

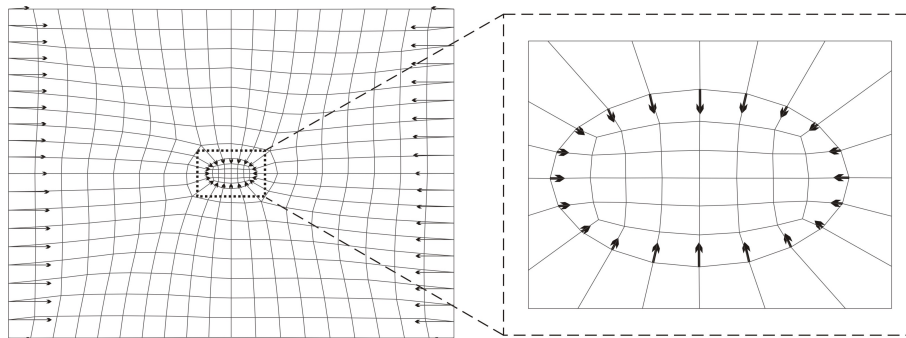


Figure 12: Configurational forces on the phase boundary of RVE

path with a maximum strain of $\varepsilon_x = 0.2$. The evolution-parameter are chosen to be $\eta = 0.01 \text{ N/mm}^2$ und $\alpha_{\rho_1} = \alpha_{\rho_2} = 250 \text{ mm}^2/\text{Ns}$. Due to the loading, no evolution in rotation has to expect. After every 0.04 s, the computation stops and the microscale will be modified. The total time of the simulation is 2.0 s. In Figure 12, the configurational forces and the structure are depicted. The arrangement of the material forces suggest an energie minimization in the case of an increased volume and an upright arrangement of the inclusion.

After modification of the nodal coordinates, the simulation ends at the following step. This procedure will repeated until the end-time of 2 s is reached. The left hand side of Figure 13 shows the initial microstructure at t_0 and, on the right, the evolved configuration after unloading (t_e). Comparison of the states before and after loading gives the modification of the inclusion. In Figure 14, geometric modifications during some chosen loading states are shown. The quantitative results are depicted in the Figures 15 and 16. The left hand side of Figure 15 shows the differences of configurational forces in x- and y-direction. The y-component of the driving force is higher than in x-component. This defines the direction of a crack propagation. The nonlinear configurational force pathes

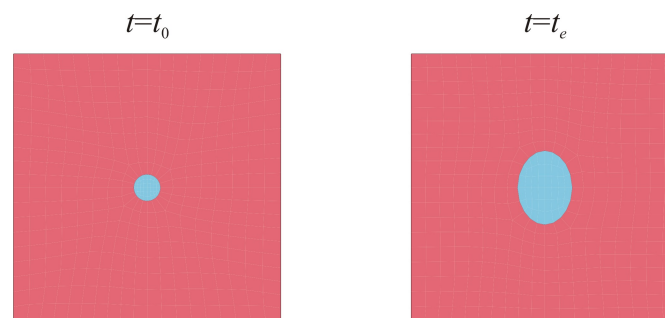


Figure 13: microstructure before and after loading

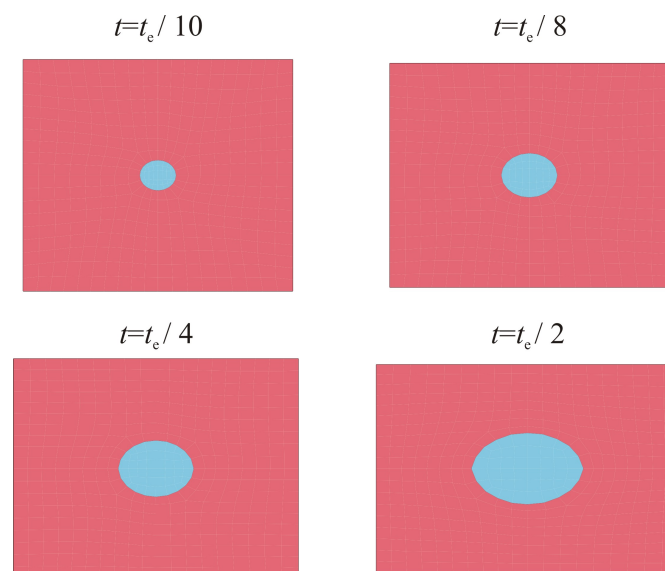


Figure 14: Microstructure at different deformation states

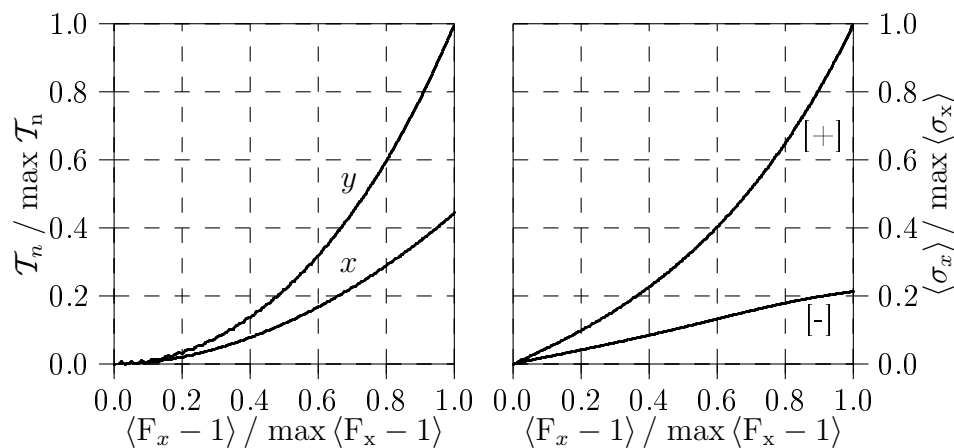


Figure 15: Configurational forces in x- und y-direction (left), averaged stress of matrix [+] and inclusion [-] in x-direction (right)

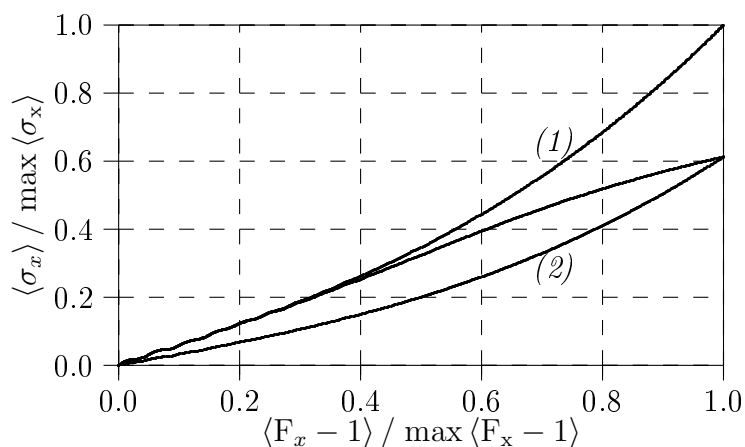


Figure 16: Averaged stress at loading/unloading with(1)/without evolution(2)

are caused by the hyperelastic material model, where the chosen parameters $C_1 < C_2$ controls an overlinear stress path. The distinct difference in averaged stress for the x-direction is shown in Figure 15.

The effect of microstructural evolution in the context of damage modelling is illustrated with Figure 16. In the case of a constant reference configuration, the loading and unloading paths are identical (path 1). In the case of evolution (path 2), the averaged stress decreases due to the increasing influence of the soft inclusion. During unloading, no evolution takes place and the unloading path coincides with the loading path of the configuration of the right hand side of Figure 13.

Although the material is isotropic in the microscale, the ellipsoidal evolution results in anisotropic overall properties. This effect is very difficult to model phenomenologically. The numerical approximation of such effects is the main advantage of twoscale-considerations. To show the anisotropic effects, we like to compare the stiffness tangents

of the damaged and undamaged pathes in Figure 16

$$\frac{\mathbb{C}^0}{C_{11}^0} = \begin{pmatrix} 1.00 & 0.42 & 0.00 \\ 0.42 & 1.00 & 0.00 \\ 0.00 & 0.00 & 0.29 \end{pmatrix} \Rightarrow \begin{pmatrix} 0.52 & 0.25 & 0.00 \\ 0.25 & 0.74 & 0.00 \\ 0.00 & 0.00 & 0.18 \end{pmatrix} = \frac{\mathbb{C}}{C_{11}^0} \quad (51)$$

Based on the undamaged (\mathbb{C}^0) and damaged (\mathbb{C}) stiffness tensors in relation (51), the anisotropic behaviour on the macroscale as an effect of the microstructural evolution can be proved: At the beginning, the macroscale has an identical stiffness in x- and y-direction. At the end, the maximum of stiffness is lost in the x-direction.

3.6.2 Anisotropic Matrix Material

In the following example, we consider a three-dimensional microstructure with anisotropic material behaviour for the matrix and the inclusion. In this case, we superimpose the anisotropic effects from both the material and the damage evolution. The initial semi-axes of the three-dimensional ellipsoid are chosen to be $a = b = c = 8.66/100$ mm and the edge length of the cube-like microstructure is 1 mm.

The inclusion is discretized with 216 solid-elements and the matrix with 1296 solid-elements. The evolution parameters are $\alpha_{\rho_1} = 100$ mm²/Ns, $\alpha_{\rho_2} = 100$ mm²/Ns and $\eta = 0.01$ N/mm². The microstructure is loaded in z-direction with fixed boundaries in x- and y-direction. The averaged deformation gradient is thus given by

$$\langle \mathbf{F} \rangle = \begin{pmatrix} 1 & 0 & 0 \\ 0 & 1 & 0 \\ 0 & 0 & 1 + \gamma(t) \end{pmatrix}. \quad (52)$$

The time-deformation-path is, again, triangular-shaped with $\max \gamma = 0.2$. The material-parameters in Equation (5) are chosen as follows: $a_1 = 0.3$ N/mm², $a_2 = 0.5$ N/mm², $a_3 = 0.0$ N/mm², $c_1 = 0.0$ N/mm², $c_2 = 0.6$ N/mm² and $c_3 - c_6 = 0.0$ N/mm². The anisotropic stiffness is activated in x-direction with $\mathbf{A}^T = [1 \ 0 \ 0]$. Poisson's ratio is given by $\nu = 0.46$ which results in a small dilatation. In Figure 17, the material forces on the ellipsoidal inclusion are depicted. The influence of the configurational forces in z-direction is negligible. However, the fixed boundaries in x- and y-direction result in a

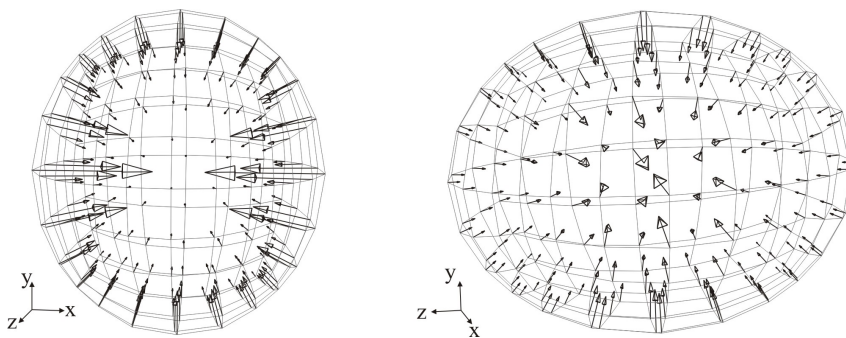


Figure 17: configurational forces at anisotropic formulation

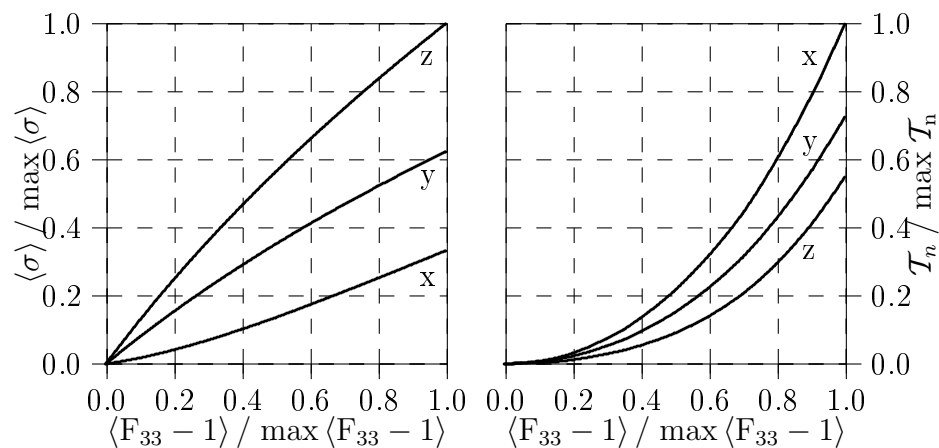


Figure 18: stress and configurational forces at anisotropic material

stress in this directions where the anisotropic material definition contracts the structure more intensively in x-direction. In the left hand side of Figure 18, the averaged stress of the microstructure is shown. The right hand side presents the paths of configurational forces at the coordinates $(a, 0, 0) \rightarrow x$, $(0, b, 0) \rightarrow y$ und $(0, 0, c) \rightarrow z$ where the evolution in x-direction dominates (these curves coincides in the case of isotropy). Figure 19 shows the different evolutions in all three directions due to the superimposed effect. This results in a change of the semi-axes from $a_0 = b_0 = c_0 = 8.66/100$ mm to $a_e \approx 30/100$ mm, $b_e \approx 25/100$ mm and $c_e \approx 20/100$ mm at the end of evolution.

The microstructural evolution shown in the previous examples is used to couple the micro- and macroscale (see TIMMEL et al. [12]). The averaged stress of the microstructure is transferred to the GAUSSIAN point of the macroscale, i.e. every integration point treats its own microstructure. The present microstructural model is capable to simulate anisotropic damage evolution. To illustrate the coupling-effect, we show a qualitative result of the two-scale procedure with an isotropic matrix material. In the centre of Figure 20, the macrostructure is shown which is loaded at the end of the cantilever by a time-depended deformation u . The initial microstructure corresponds to the systems shown on the upper

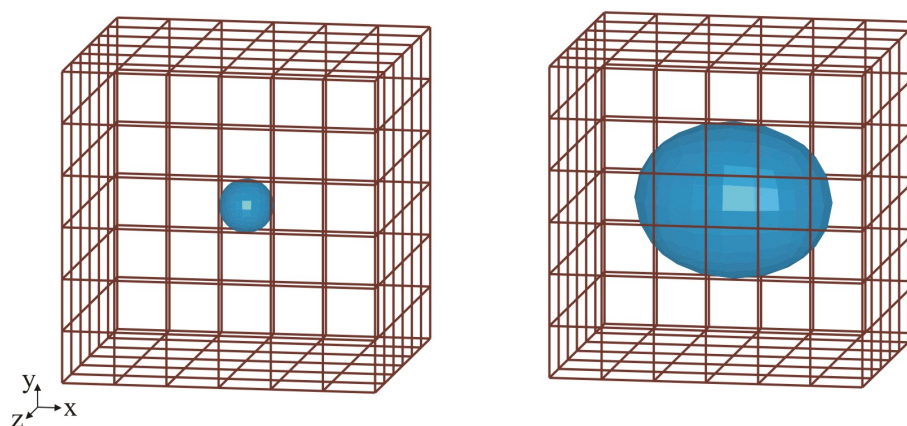


Figure 19: Undeformed Microstructure before/after loading

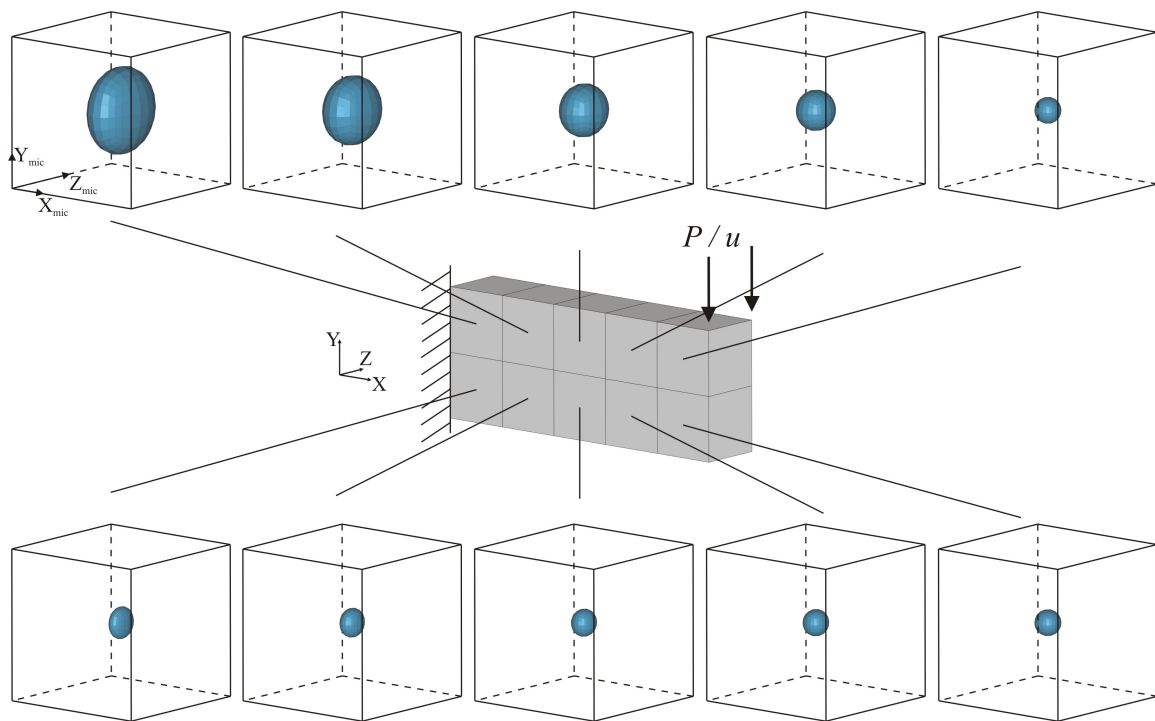


Figure 20: Undeformed micro- and macroscale after unloading

or lower right hand side of Figure 20 where no evolution takes place due to the slow lever arm and the chosen evolution parameter.

At the upper left side, the maximum of the evolution is obtained. Here, an evolution in volume and in the shape of the inclusion takes place. In the counterpart, the lower left side of the cantilever shows a modification in shape, but no evolution in volume. This fact is caused by Equation (38), where the volume evolution is suppressed in the case of compression. As a consequence of the entire evolution process, the macrostructure evolved from isotropic properties to anisotropic one.

4 Conclusions and Outlook

The present article contains the modeling technique of anisotropic effects in rubber-like materials. In this context, we distinguish between phenomenological and micromechanical models. A phenomenological model is used to simulate a directional stiffness which is by the structural geometry.

The micromechanical model is used to describe the physical behaviour during the loading process in more detail. This computational technique is able to describe both anisotropy and softening effects which are induced by the evolution process in the microscale. A two-scale approach is presented where the evolution of damage is modelled by the evolution of soft ellipsoids representing the damaged zone. It is shown how the initially isotropic properties are lost during the loading process. Moreover, we also applied the two-scale damage approach for anisotropic material behaviour in the microscale. This represents a

first step for the simulation of reinforced structures or composites where the anisotropic effects induced by material properties and damage evolution are superimposed.

The present computational model is not restricted to hyperelasticity but is also suitable for the modeling of inelastic materials. In particular, rate-dependent elasto-plastic materials will be a topic of further investigations.

References

- [1] ESHELBY, J. D.: Energy relations and the energy-momentum tensor in continuum mechanics. *In Kanninen M.F.: Inelastic behaviour of solids*, Mc Graw Hill, New York, pp. 87-122, 1970.
- [2] KALISKE, M; ANDRE, M; RIEGER, A.: Modelling of Structural Inhomogeneities by a Homogenized Approach, *Proceedings of the Third European Conference on Constitutive Models for Rubber*, London, 2003.
- [3] KALISKE, M; SCHMIDT, J.: Modelling and Implementation of Nonlinear Anisotropic Elasticity into ANSYS, *Report 05-2004*, Institute for Structural Mechanics, University of Leipzig, Leipzig, 2004.
- [4] KALISKE, M; TIMMEL, M.: Representation of geometric structural pattern in elastomeric solids by a non-linear anisotropic model, *Plastics, Rubbers and Composites* 34 (2005) 357-364.
- [5] KOLLING, S.: Zur numerischen Simulation von Morphologieänderungen in mikroheterogenen Materialien. Institute of Mechanics, University of Darmstadt, Darmstadt, 2001.
- [6] LOEHNERT, S.: Computational Homogenization of Microheterogeneous Materials at Finite Strains Including Damage. Institut für Baumechanik und numerische Mechanik, Universität Hannover, Hannover, 2004.
- [7] MAUGIN, G.A.: Material Inhomogeneities in Elasticity. *Chapman and Hall, London, 1993*.
- [8] MUELLER, R.: 3D-Simulation der Mikrostrukturentwicklung in Zwei-Phasen-Materialien. Institute of Mechanics, University of Darmstadt, Darmstadt, 2001.
- [9] NEMAT-NASSER, S.: Averaging theorems in finite deformations plasticity , *Mechanics of Materials* 22 (1999) 493-523.
- [10] SCHMIDT, I.: Gleichgewichtsmorphologien elastischer Einschlüsse, Institute of Mechanics, University of Darmstadt, Darmstadt, 1997.
- [11] SPENCER, A.J.M.: *Continuum Theory of the Mechanics of Fibre-Reinforced Composites*, CISM Courses and Lectures, No. 282, Springer-Verlag, Wien, 1984.

- [12] TIMMEL, M.; KALISKE, M.; KOLLING: Damage Simulation based on a Two Scale Approach, *Proceedings of the 5th LS-DYNA Forum*, Ulm, Germany (2006) D-II, 33-47.
- [13] TIMMEL, M.; KALISKE, M.; KOLLING, S.; MUELLER, R.: A Micromechanical Approach to Simulate Rubberlike Materials with Damage, *Computers, Materials and Continua* 5 (2007) 161-172.
- [14] YEOH, O.H.: Characterization of Elastic Properties of Carbon-Black-Filled Rubber Vulcanizates, *Rubber Chemistry and Technology* 63 (1990) 792-805.